AUTOMATIC CANINE MUSCLE HISTOLOGY IMAGE SEGMENTATION BASED ON RGB HISTOGRAM

A Thesis

by

STEPHEN CRAIG MCCONNELL

Submitted to the Office of Graduate and Professional Studies of
Texas A&M University
in partial fulfillment of the requirements for the degree of

MASTER OF SCIENCE

Chair of Committee,	Jim Ji
Co-Chair of Committee,	Robert Balog
Committee Members,	Joe Kornegay
	Tie Liu
	Ulisses Braga-Neto
Head of Department,	Miroslav Begovic

May 2017

Major Subject: Electrical Engineering

ABSTRACT

Duchenne muscular dystrophy is a fatal, congenital disease affecting males. Histopathological methods have served to aid in its diagnosis; however, the ratio of skeletal muscle tissue constituents—a theoretical marker of the disease—has yet to be rigorously quantified. An automatic histology image segmentation algorithm was developed in this work to quantify the collagen to muscle fiber ratio occurring in 11 muscle samples from golden retriever muscular dystrophic animals. Preliminary artifact removal and segmentation of myosatellite cells was included. Additionally, the effect of altering the processing resolution was studied on the outcome of the collagen to muscle ratio. In comparison with estimations from a repurposed industry software, Aperio ImageScope, the custom algorithm was faster and less susceptible to artifact. However, processing resolution increased execution time and had significant effects on the collagen to muscle ratio for both algorithms. An optimal processing resolution was suggested.

ACKNOWLEDGEMENTS

I would like to thank my committee chair and co-chair, Dr. Ji and Dr. Balog, and my committee members, Dr. Kornegay, Dr. Liu, and Dr. Braga-Neto, for their guidance and support throughout the course of this research.

Thanks also go to my friends and colleagues, especially Sharla and Aydin, for their assistance, and the department faculty and staff for making my time at Texas A&M University a great experience.

Finally, thanks to my wife for her patience and love.

CONTRIBUTORS AND FUNDING SOURCES

Contributors

This work was supervised by a thesis committee consisting of Professor Jim Ji, chair, Professor Robert Balog, co-chair, and committee members Professor Tie Liu and Professor Ulisses Braga-Neto—all of the Department of Electrical & Computer Engineering and Professor Joe Kornegay of the Department of Veterinary Integrative Biosciences.

Training in the identification of degenerate fibers, and the muscle, fibrosis, and fatty tissue distinctions was provided by Sharla Birch, DVM and licensed pathologist. She also provided to me the parameters for use with Aperio ImageScope, was the primary supplier of the image samples used throughout the study, and proof read much of the final thesis draft.

Aydin Eresen brought to my attention a few resources including extant literature and software.

All other work conducted for the thesis was completed by the student under the advisement of the committee members listed above.

Funding Sources

There are no outside funding contributions to acknowledge related to the research and compilation of this document.

NOMENCLATURE

DMD	Duchenne Muscular Dystrophy
GB	Gigabyte(s)
GRMD	Golden Retriever Muscular Dystrophy
JPEG	Joint Photographic Experts Group compression standard
MRI	Magnetic Resonance Imaging
NDPI	NanoZoomer Digital Pathology Image format
RGB	Red, Green, Blue color model
TIFF	Tagged Image File Format

TABLE OF CONTENTS

Page

LIST OF FIGURES

Page

1. INTRODUCTION AND APPROACH

1.1 Introduction

Duchenne muscular dystrophy (DMD) is a disease that "usually leaves affected boys severely disabled by their early teenage years, and results in death due to respiratory and cardiac failure" [1]. In effort to study, diagnose, and offer earlier treatment for this fatal muscular disease affecting about 1 in 3500 live born males [2], a canine colony exhibiting golden retriever muscular dystrophy (GRMD) is kept at the College of Veterinary Medicine at Texas A&M University. The canine condition is the closest known animal model of the human pathology phenotypically in addition to pathologic similarity [3].

As both DMD and GRMD progress, the primary constituents of muscle tissue—collagen, fatty deposits, and muscle cells—change in their relative abundance with respect to one another [4]. Fibrosis, or the abnormal deposition of extra cellular matrix components (predominantly collagen), serves to add structure to atrophying muscle tissue, yet it is substituted for and may eventually inhibit regrowth of skeletal muscle [5]. Quantifying the percent composition of the skeletal muscle tissue in a given sample in terms of its fibrosis and fatty deposits versus muscle cells may therefore indicate the presence and/or status of progression of the disease.

Histological examination has long served as the gold standard for pathological diagnoses of DMD. However, the bulk elements of histology have yet to be rigorously quantified as to their relative proportions at the macroscopic level. Doing so not only

allows for a less qualitative interpretation of the degree of fatty and fibrotic tissue infiltration as histological markers, but potentially paves the way for the use of less-invasive MRI assessments in therapeutic interventions by enabling comparison of quantified tissue data.

The scope of this work is to process high resolution images of GRMD canine pectineus muscle histology samples in order to quantify the amount of fibrosis, interstitial tissue (which includes fatty deposits), and skeletal muscle. In particular, this study not only compares the relative amounts of these tissue constituents across 11 GRMD canine samples, but also examines the effect of processing the sample images at different resolutions.

In order to process these images a custom algorithm was written which leverages tissue color information enhanced by a trichrome stain. The results of this algorithm are compared to results obtained using Aperio ImageScope, an industry digital pathology software, that was adapted for quantifying the tissues of interest. This latter software has been commonly employed for tissue classification and quantification in studies involving immunology [6-8] and even image segmentation of angiogenesis [9], although not particularly for muscle histology.

1.2 Segmentation Approach

The purpose of trichrome staining is to stain fibrosis, composed of collagen proteins, blue and to leave the surrounding muscle cells red or pink. The fat cells are left mostly translucent or white against the background of the slides. Together fibrosis, skeletal muscle, and fat form the three major constituents of the muscle tissue. Non-

tissue, or clefting of the muscle tissue that reveals the slide background, can also show through often in white veins throughout a sample.

With a quick glance at Fig. 1a the dominant red, blue, and white colors are apparent. The segmentation strategy in this work was to exploit the differences in the RGB color space to separate out the muscle, fibrosis, and interstitial or white component that includes both clefting and fatty tissue. While the decision to lump tissue and non-tissue together may at first seem counterintuitive, it was justified by trained pathological manual segmentation by one of the authors that the amount of fatty deposits were usually both small and difficult to distinguish from the background, even for the trained eye.

Morphological image processing was attempted initially to aid in the recognition of circular or ovoid shapes—specifically in effort to locate the round, white fat cells, but eventually this approach to identify tissue categories was abandoned for multiple reasons. First, it introduces inevitable quantification error by unintentionally growing or shrinking the relative size of the tissue constituent regions, e.g., through dilation and erosion operations. These regions initially began as RGB threshold regions without defined shape but were altered morphologically to fit some predefined intuition of cell size and shape. Second, attempting to track the additional error introduced by the morphological operations, i.e., tracking all of the pixels that were modified by any single operation or by multiple operations also significantly decreased the efficiency of the algorithm, especially with the prodigious image size playing a role. Third, muscle fibers, fat, and fibrosis do not always have a consistent shape, so using opening and closing

operations to look for round objects often proved ineffective when the shapes occurred frequently in asymmetric, oblong form. These erratic shapes are especially prevalent because the requisite slicing of the tissue is seldom a perfect normal cross-section and unavoidable slicing deformations are introduced in the sub-tissue constituents. And finally, extensive morphological operations including geometric computations increased execution time. Despite all of these disadvantages for full-scale image processing, however, morphological operations were used at low resolution to help form the tissue border mask.

A combination of watershed transformations and semi-manual techniques [10] and a gradient vector flow deformable model incorporating seed regions [11] have been used to try to identify muscle fibers based on shape and/or exploiting the natural fiber boundary lines created by the surrounding endomysium. However, close observation of the data acquired in this study revealed that often the endomysium was so thin in certain regions that only partial boundary lines around individual fibers could be detected. The overwhelming abundance of such occurrences made semi-manual segmentation impractical. Furthermore, this study aimed not to isolate and quantify the number and/or size of the muscle fibers but aimed to consider the extent of the non-uniform fibrosis and fat infiltration relative to the total cross-sectional area of the muscle fibers in healthy as well as diseased tissue. Other manually intensive or supervised learning techniques could not be employed for burden of acquiring manually segmented data on images of the immense size and fine resolution as detailed in the following section.

For the preceding reasons detailed, a strictly color-based automatic threshold setting algorithm was employed in this work to differentiate between histological tissue constituents.

1.3 Acquisition Method

Pectineus muscles were harvested from 11 post-mortem GRMD animals. The muscles were sliced in the transverse plane at the approximate midpoint along the length of each specimen. Two slices were acquired from the left and right faces of the midpoint, although in this study only the left face was used. The slices were acquired with a microtome at a thickness of 5um. Each pair of slices was mounted onto a white slide and a trichrome stain was applied to enhance collagen pigment (see Fig. 1(a)).

The slides were scanned with a Hamamatsu NanoZoomer 2.0-HT scanner at 40x optical zoom or equivalently at a resolution of 227nm per unit length of each pixel. The scanned images each represented an area of approximately 50 x 25 mm. Uncompressed, the images individually contained from 18 to 24 billion pixels. At the high end, this is the equivalent viewing area of approximately 11,440 modern computer screens (1920 x 1080 pixels). The image files from the NanoZoomer digital scanner were stored in a proprietary NDPI file format (similar to TIFF) that assigned RGB color information for each pixel. The compressed file sizes ranged from 1 to 4 GB.

All processing was performed on an Asus ROG G750 laptop with a 2.40GHz Intel Core i7 processor and an NVIDIA GeForce GTX 860M graphics processing unit using Microsoft Windows 8 64-bit and MATLAB R2016a. Alternate processing for

validation purposes was performed in Aperio ImageScope software (version 12.2.2.5015) by Leica Biosystems.

2. STEPS IN PROCESSING

2.1 Image Partitioning and Downsampled Copies

Using the **ndpisplit** function provided by work done by Deroulers *et al* [12], each image was converted from NDPI to TIFF using lossless compression. Additionally, the function split the images into a 16x32 partition of equal-sized pieces or sub-images. The utilization of the partition of sub-images was necessary to enable efficient image processing in MATLAB which enforces limitations on memory allocations.

This partitioning process was completed at the original resolution as well as at resolutions $1/4^{th}$, $1/16^{th}$, and $1/64^{th}$ of the original (compressed along both dimensions), equivalent to 10x, 2.5x, and 0.625x optical zoom. For the latter resolutions, the down-sampling was accomplished using JPEG compression [12], but the resulting images were converted again to lossless TIFF.

2.2 Mask Creation

After the images were converted to a known file format, they were imported to MATLAB for further processing. Before the sample images could be analyzed in terms of their tissue constituents, it was necessary to separate the background pixels from those containing real tissue information. Additionally, only the left-hand side sample of each slide was to be used.

The sample mask formation was accomplished in four steps. First, the $1/64^{th}$ resolution image was converted from color to grayscale and then further to black and

white using an internal MATLAB function based on Otsu's method. Second, a logical margin mask was applied which cropped 10% of the total image rows from each of the top and bottom, 15% of the total columns from the left-hand side, and 40% of the total columns from the right-hand side, see Fig. 1(b). The main function of this mask was to eliminate the right-hand side sample and remove lines appearing around the edges of the image from the rectangular slide. Third, morphological operations were employed to erode away extraneous tissue from around the sample and to obtain the approximate shape of the mask. Fourth, active contours implemented by an internal MATLAB method with the parameter of 150 iterations refined the boundary along the edges of the sample. Fig. 1 illustrates these steps including the final binary mask.

This completed mask was saved to file and subsequently re-imported to MATLAB where it was partitioned into 16 rows and 32 columns of equally sized images. MATLAB then fetched the corresponding RGB images from the sample partition at the full resolution, excluding those that were associated with purely background (black) in the mask. The sub-images from the binary mask were then scaled to the size of the full-resolution sub-images one at a time, and the binary mask was applied to each full-resolution sub-image to remove RGB information located outside the border of the sample.

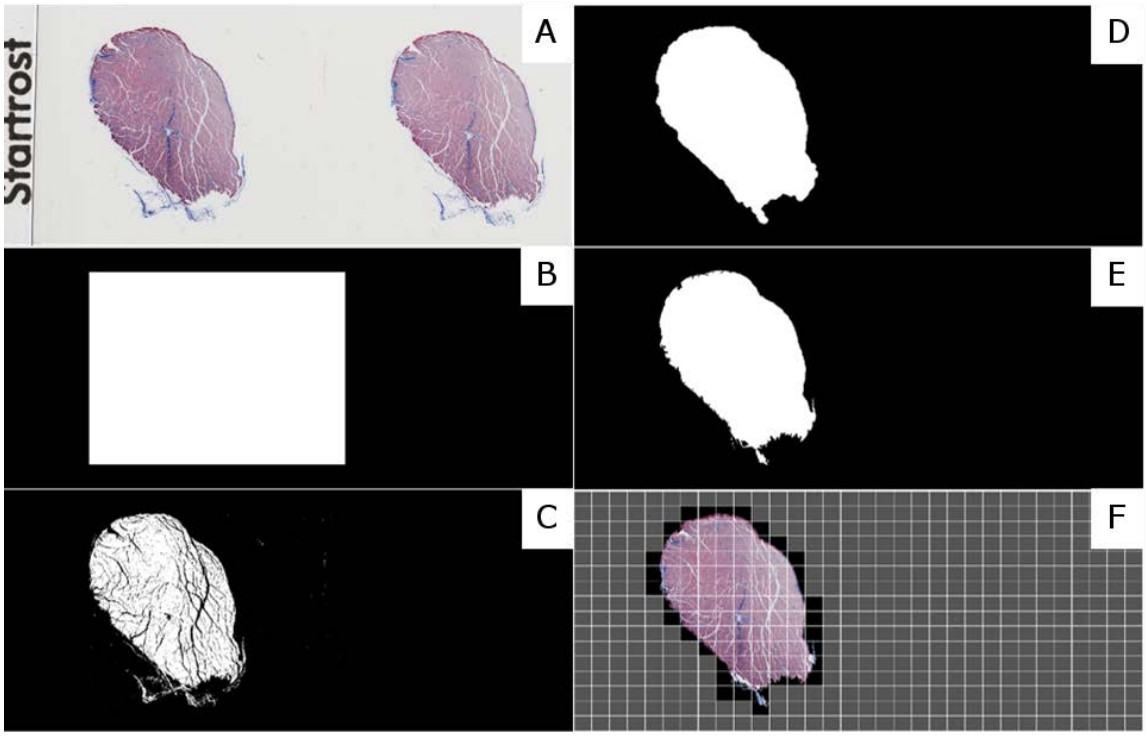

Figure 1. Mask creation: a) Original scanned slide downsampled to 1/64th resolution (not actual size); b) Logical margin mask; c) Binarized image post logical mask; d) Sample mask after morphological erosion and closing; e) Final mask after active contour fitting; f) 16x32 processing partition shown superimposed on final masked image. Partition blocks void of information after the mask are shaded gray.

2.3 Histogram Analysis

The segmentation thresholds were designed based on detailed observational study of image histogram shape in comparison with sampled values from common image features. For example, in separating the white interstitial space from the skeletal muscle fibers and collagen, it was observed that sampled pixel values from the interstitial space almost exclusively belonged to a particular upper portion of the intensity values in the RGB histogram.

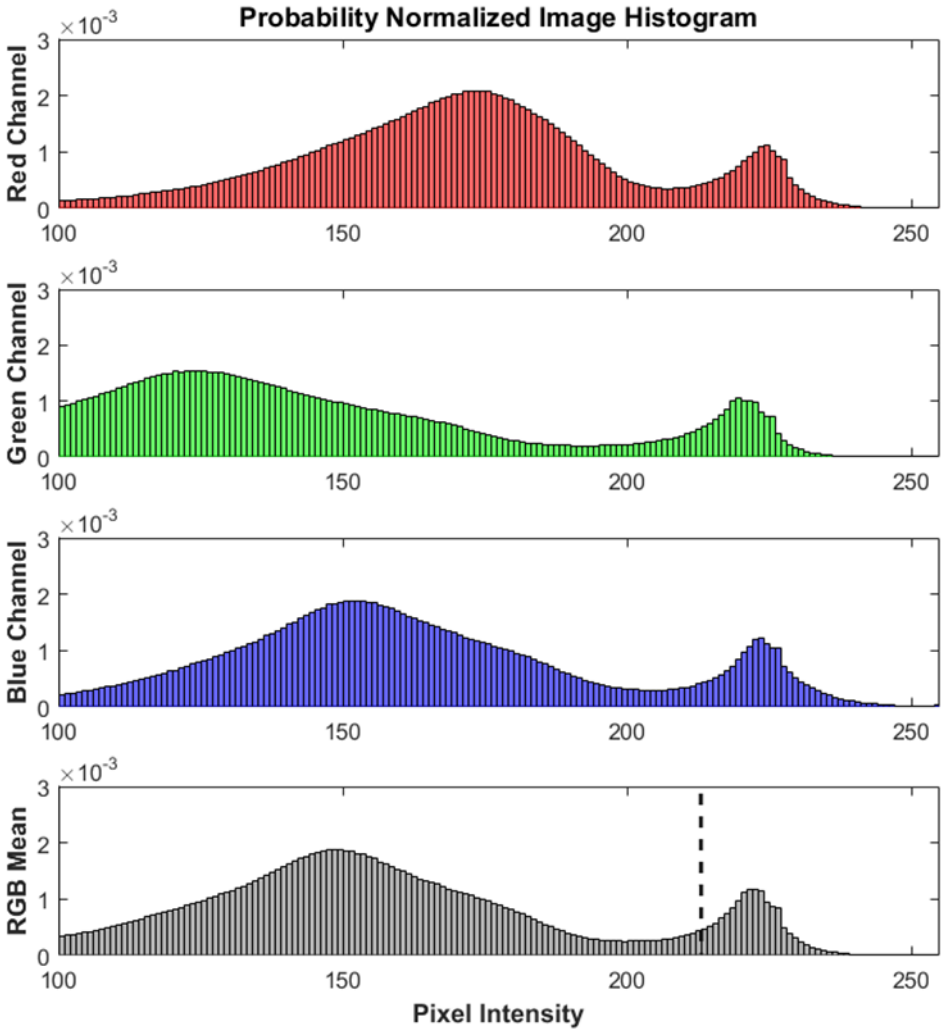

Figure 2. From top to bottom: image histogram with intensity levels from 100 to 255 for the red, green, and blue channels and then the mean of the three channels, respectively. The dotted line represents the interstitial/non-interstitial threshold.

Fig. 2 displays the image histogram for sample 6 in terms of red, green, and blue components. The average of the three channels is shown below in gray. Specific to this sample, but highly similar among all samples, is the threshold depicted by the dashed line in Fig. 2. This threshold represents the intensity level above which the white interstitial space belongs.

The threshold itself was set dynamically for each sample using a specialized method originally introduced as a histogram based “global search threshold” in [13], but is hereafter referred to as the “triangle method”. This method finds the knee of a curve on an interval by calculating the coordinate on the curve that has maximum distance from an imaginary line segment drawn between the two interval end points. The distance from any point, *p*, on the curve to the imaginary line between endpoints *a* and *b* is calculated according to the following formula [14]:

$$D = \frac{\|\overrightarrow{ab} \times \overrightarrow{ap}\|}{\|\overrightarrow{ab}\|} = \left|x_p \Delta y_{ab} - \Delta x_{ab} y_p + x_b y_a - x_a y_b\right| / \sqrt[2]{\Delta x_{ab}^2 + \Delta y_{ab}^2} \qquad (1)$$

In this case, the method was employed by choosing the point of the peak on the right and the local minimum to the left of the dashed line as the endpoints.

The triangle method was verified empirically for accuracy against the more renown Otsu’s method as shown in Fig. 3. The aim of Otsu’s method is to maximize interclass variance or spacing between two distributions [15]. However, in this case, it proves less effective at finding an appropriate threshold between the white interstitial space and the remaining colored tissue automatically. This can be attributed to the fact that Otsu’s method does not actually acquire perfect knowledge of the distribution of the two classes underlying the data, and particularly in the tail areas, the histogram leaves the overlapping region between the two classes completely ambiguous. The result, shown in the bottom of Fig. 3, is that many muscle tissue pixels with lower intensity are classified with the interstitial space, particularly on the right hand side of the image.

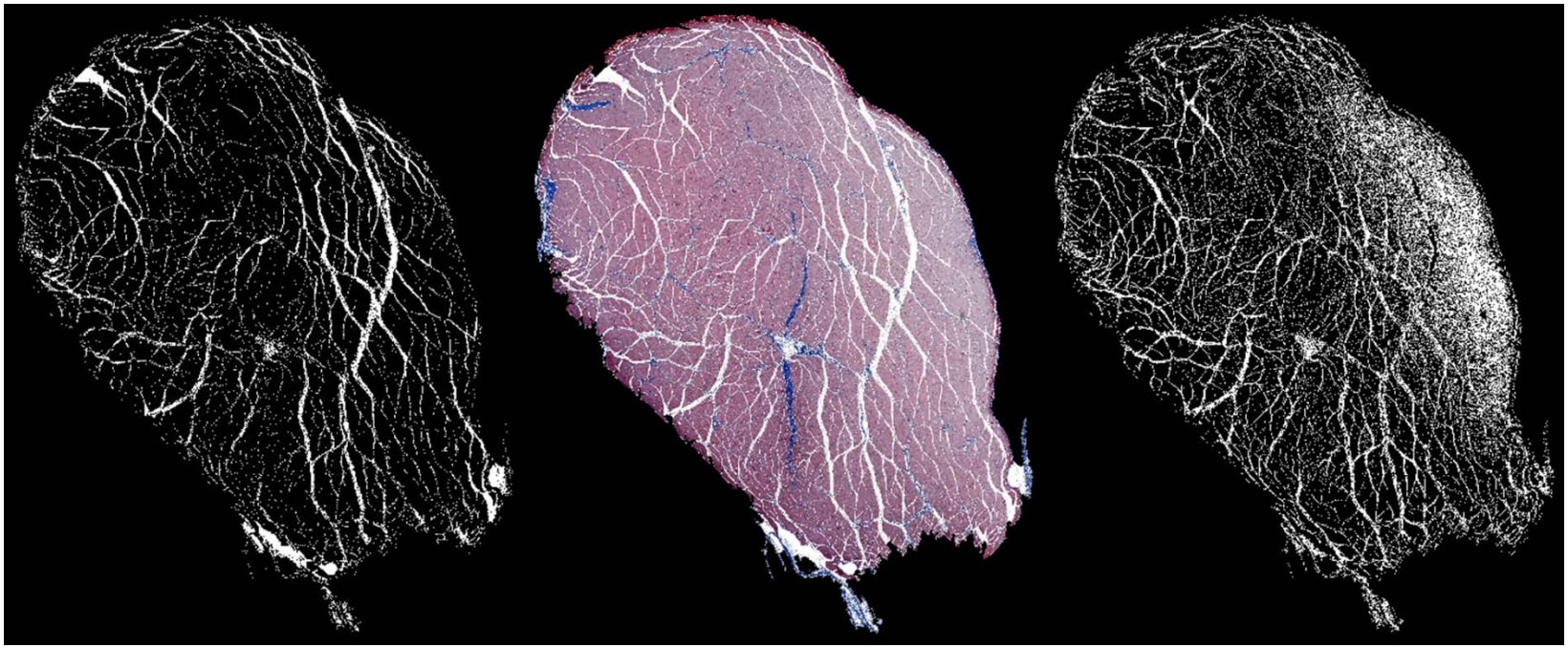

Figure 3. Left: Triangle method interstitial segmentation. Middle: Unsegmented histology image (sample 6). Right: Otsu's method interstitial segmentation.

The present implementation of the triangle method, on the other hand, assumes that the tail of the interstitial distribution to the left of the threshold in Fig. 2 (just beyond the knee point in the interstitial class curve) is much less significant than the tail of the left-hand side distribution containing the bulk of the muscle/fibrous tissue or non-interstitial space. Empirical qualitative validation (like the results in Fig. 3) with various segmentation thresholds has verified this assumption.

2.4 Separating Fibrosis from Muscle

With the understanding that the vast majority of the pixels to the left of the threshold must belong to the non-interstitial tissue category, the next step is to further divide the muscle tissue from the surrounding collagen.

Fig. 4 shows a 2-dimensional histogram of sample 6. It is evident that the largest concentration of pixels have intensities for the red and blue channels in near equal proportions, or close to a 1:1 ratio along the diagonal. Fig. 5 is a one-dimensional view of this same phenomenon, specifically tallying the ratio of blue to red for all pixels. The left-hand side of the distribution in Fig. 5 represents the muscle cells that have higher red pigment than blue. Near the value unity there is a peak which is strongly contributed to by the interstitial or white pixels which are comprised of RGB colors in approximately equal ratios. Finally, as the distribution tapers off to the right, the pixels begin to represent the fibrosis which has a higher blue component than red. Experiment showed that the triangle method was again effective at finding a suitable threshold near the knee of the curve on the right-hand side.

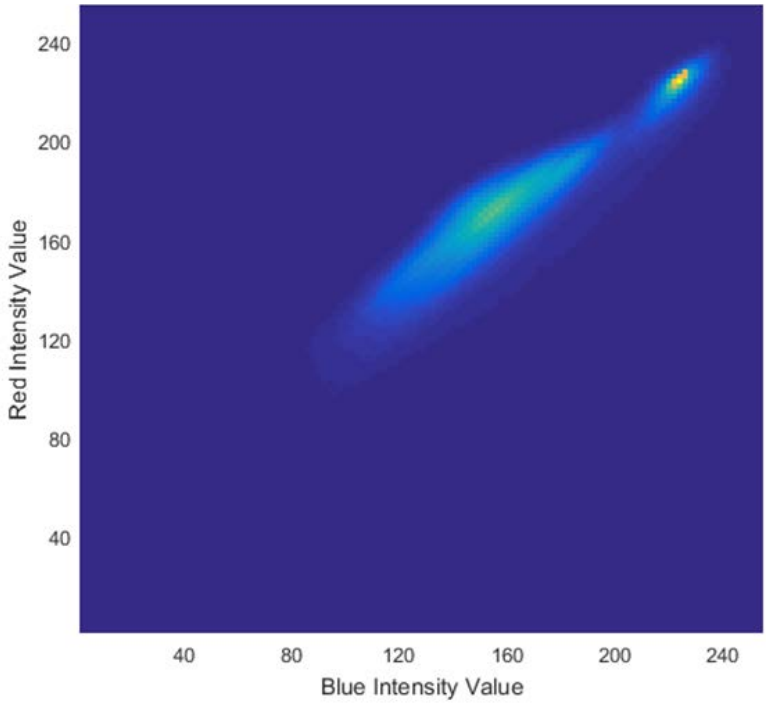

Figure 4. 2D histogram with pixel information from red and blue channels of the unsegmented image. Lowest relative abundance is shown in dark blue shown vs. highest in yellow.

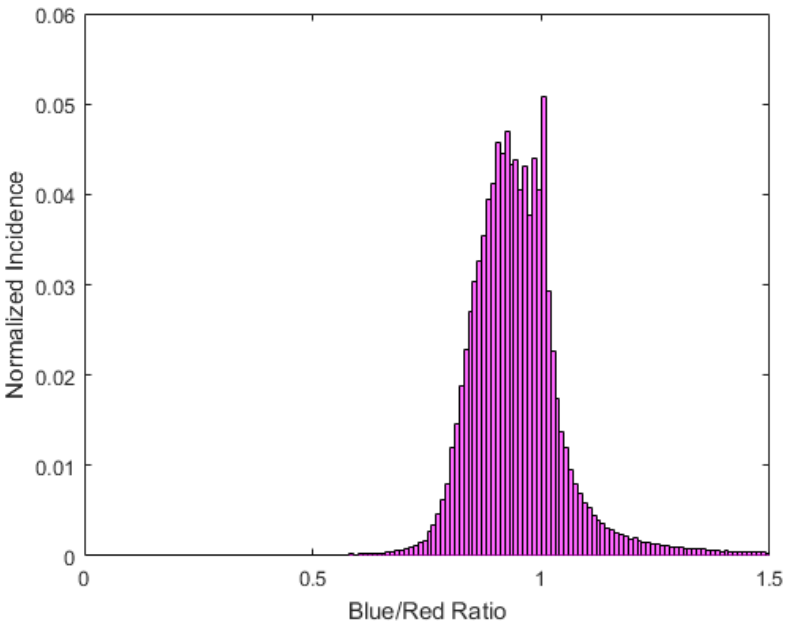

Figure 5. 1D histogram with pixel information collected after dividing the blue channel of the unsegmented image by the red.

2.5 Myosatellite Cells and Artifact Removal

In addition to segmenting the fibrosis and muscle cells from the interstitial tissue, there are a large number of myosatellite cells and artifacts which account for some 3-7% of the imaged tissue.

While the myosatellite cells could be lumped together categorically with the muscle cells that they encompass, this treatment might be counterproductive to the aim of the segmentation. Specifically, it is known that muscle cells continue to decrease in proportion to the other tissue as DMD progresses. Conversely, the myosatellite cells proliferate and become increasingly active during early progression of the disease in an attempt to regenerate dying muscle cells [16]. Therefore, studies looking at the relative proportion of muscle tissue quantified with respect to the remainder of the histological sample may find the inclusion of myosatellite cells to be a confounding factor.

Since the myosatellite cells appear darkly colored on the histology slide, it is actually convenient to remove them and dark artifacts (such as stain artifacts and small, ambiguous regions of overlapping muscle and collagen) with a single threshold located on the far left tail of the image histogram. Fig. 6 demonstrates this threshold.

Another threshold is employed which removes pixels that have very high intensity red in comparison with the other channels. This is done to remove parts of blood vessels that occasionally present themselves in the samples.

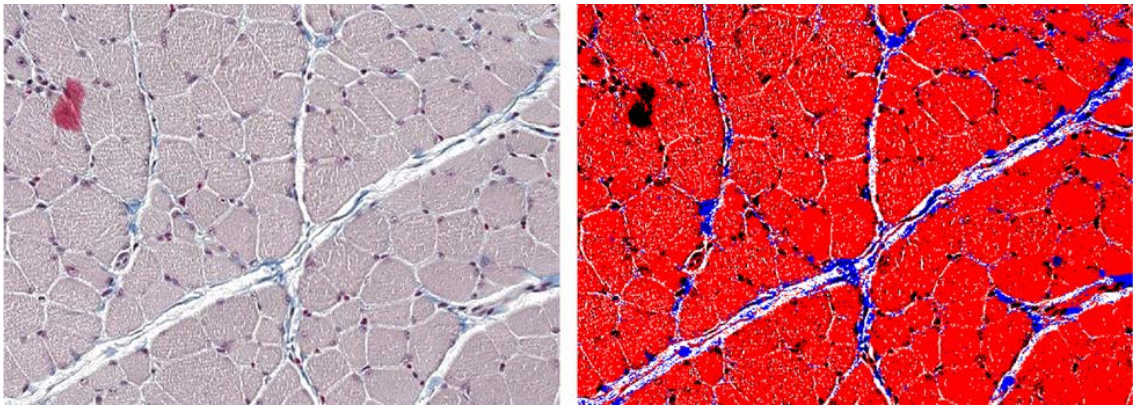

Figure 6. Left: image before segmentation. Note red stain artifact in upper left corner. Right: Segmented image, including myosatellite cell and artifact threshold. Muscle is shown in red, fibrosis blue, interstitial white, myosatellite cells and the artifact in the upper left are shaded black.

2.6 Estimation of Segmentation Error

While the described segmentation method provides a quantitative estimation of constituent tissues for all samples under study, it lacks any measure or estimation of the inevitable segmentation error. The interstitial category consistently has a segmentation result that qualitatively matches cleanly with visual expectation; however, the interstitial category has error inherent in the clefting that comes with tissue cutting, which varies considerably from sample to sample, making this tissue category a poor indicator of the amount of fatty deposition in the muscle sample.

This fact causes the quantitative measures of the fibrosis and skeletal muscle categories to be of greater interest, especially in their relative proportions to one another. Thus the ratio of fibrosis to muscle is studied specifically.

The most significant source of error affecting the ratio of fibrosis to muscle is the previously described threshold designed to distinguish them. This threshold was found to

be quite sensitive, in that slight numeric adjustment would produce non-negligible effects in the fibrosis to muscle cell ratio. Because this threshold was designed using a histogram of the blue to red channel intensity ratios, the adjustments to the threshold were quantized in increments of the histogram bins, which have a unitless width of 0.01.

Using the same approach discussed previously, which relies on finding the knee in the curve using the triangle method, two alternative threshold estimates--one higher and one lower than the initial threshold--were produced by selecting an alternative threshold bin to the left or to the right of the original, respectively. Specifically, 3 bins up the steep slope to the left of the original or down to the right to the bin representing 1/5th of the height of the original were chosen. These seemingly arbitrary cutoffs were selected based on empirical observations of visual perceptible differences in the segmentation results that appeared to represent near overestimations or underestimations of the fibrosis. While these thresholds are inherently subjective, they are presented in Fig. 7 with visual justification.

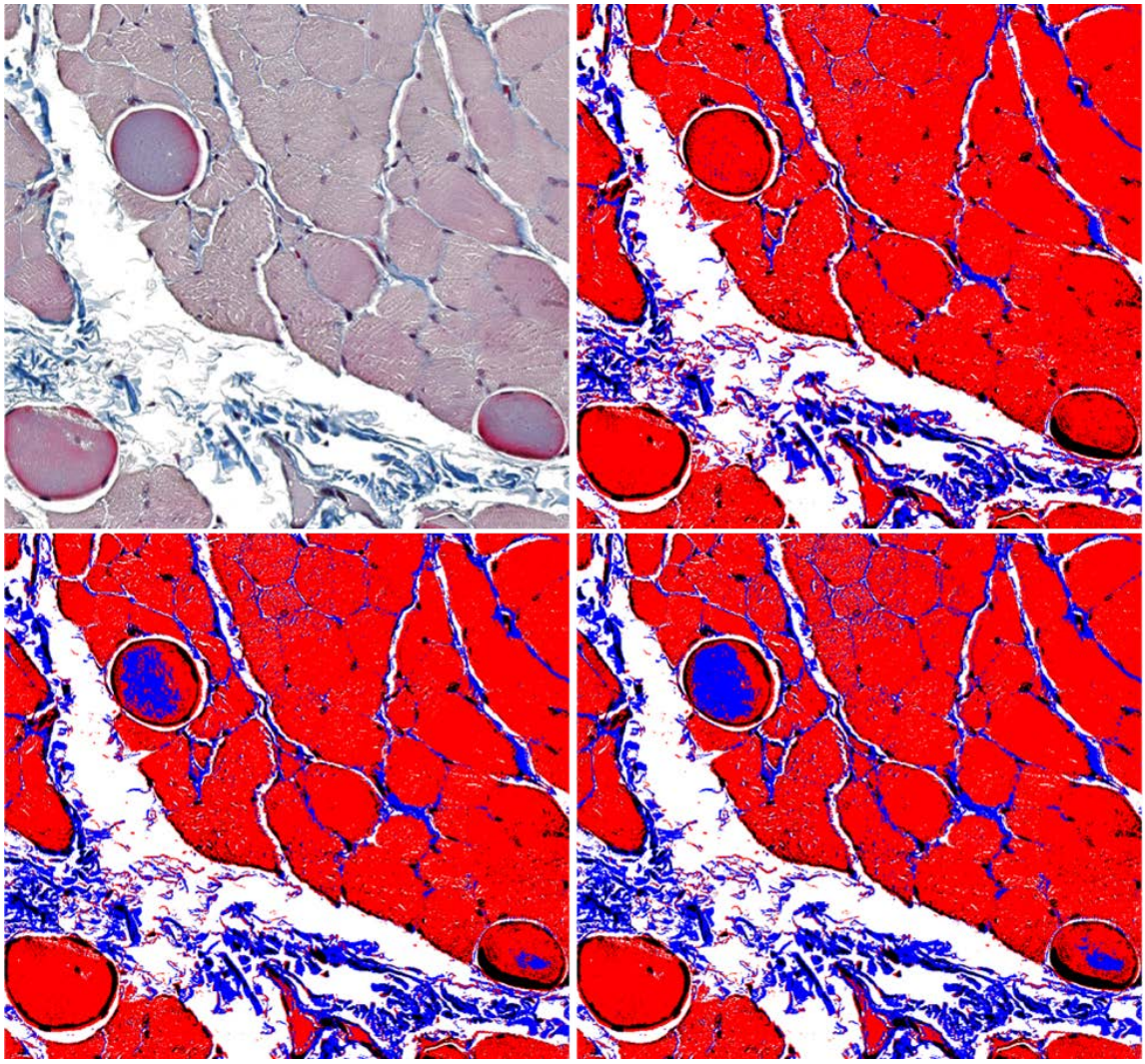

Figure 7. Top-left: image before segmentation. Top-right: image with low fibrosis estimate. Bottom-left: image with medium fibrosis estimate. Bottom-right: image with highest fibrosis estimate. As in the previous figure, muscle is shown in red, fibrosis blue, interstitial white, myosatellite cells and ambiguously dark pixels (potential artifact) are shaded black.

The low estimate in Fig. 7 is shown in the top-right. This estimate shows no obvious misclassification of tissue. However, when compared with the higher estimates and the original image, it is clear that this threshold underestimates the collagen of the endomysium surrounding individual muscle fibers. The high estimate, shown in the

bottom-right, shows the strongest measurement of the endomysium with more visible and complete collagen lines between skeletal muscle fibers, but it also has an obvious overestimation where a degenerating muscle fiber is shown to be collagen. The bluish appearance of this degenerating fiber in the original image is not because of fibrosis, but likely due to processes associated with cellular mineralization and necrosis associated with the GRMD pathology. Unfortunately, this color appears equivalent to much of the endomysium that the algorithm intends to measure. A compromise is therefore made between the high and low estimates resulting in the image shown at the bottom-left of Fig. 7.

This system of three estimates was computed for every pixel in each of the samples in the study.

3. RESULTS

3.1 Examining Segmentation Results at Different Resolutions

The algorithm detailed up to this point described the process of segmenting the images at the full resolution provided by the Hamamatsu scanner. However, it is of interest to understand how lower scan resolution or loss of resolution may affect the tissue quantification results.

Processing the images at lower resolutions than the maximum was initiated by downsampling the full resolution images as mentioned previously. An image partition like the one shown in Fig. 1(f) was again created, but with fewer rows and columns depending on how far the image was downsampled. The remaining segmentation steps—including the automatic determination of the thresholds—were virtually identical to those described previously for the full resolution.

The results of processing the images at resolutions 1/4th, 1/16th, and 1/64th of the original are shown in Fig. 8. Note that sample 7 is omitted from the results due to incorrect scanning procedures. Note also that the 1/4th, 1/16th, and 1/64th designations represent the reduction in pixel count along a single dimension, such that the image pixel area is actually reduced by 1/16th, 1/256th, and 1/4096th of the original. Not surprisingly, the algorithm execution time decreases dramatically at the lower resolutions as shown in Fig. 9.

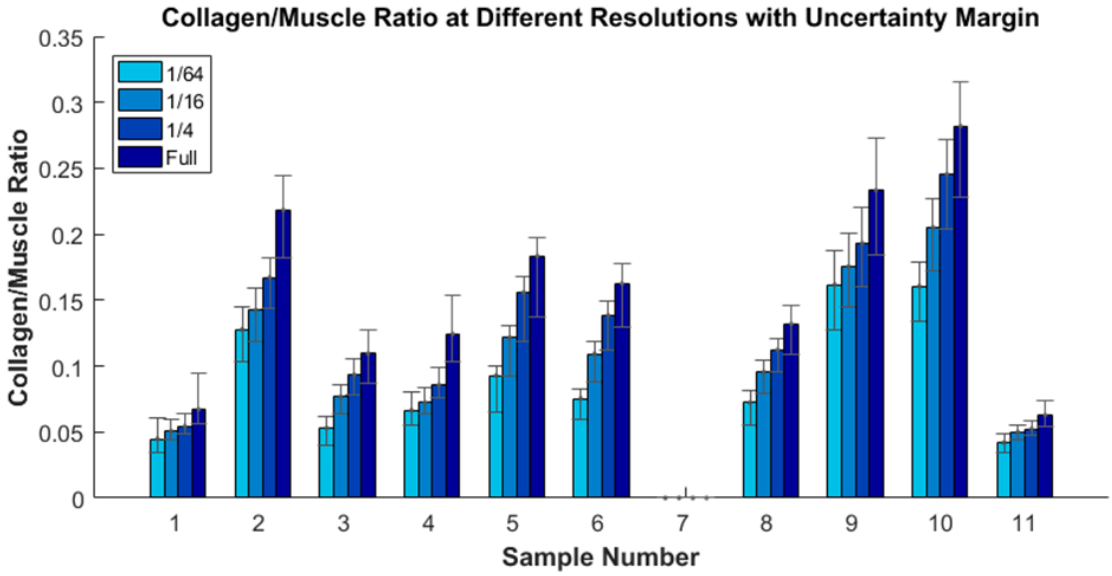

Figure 8. Collagen to muscle ratio for each sample with increasing resolution. The labels 1/64, 1/16, and 1/4 represent the scaled reduction in pixels along both dimensions. In other words, the label "1/64" means 1/64 height and 1/64 width of the full resolution.

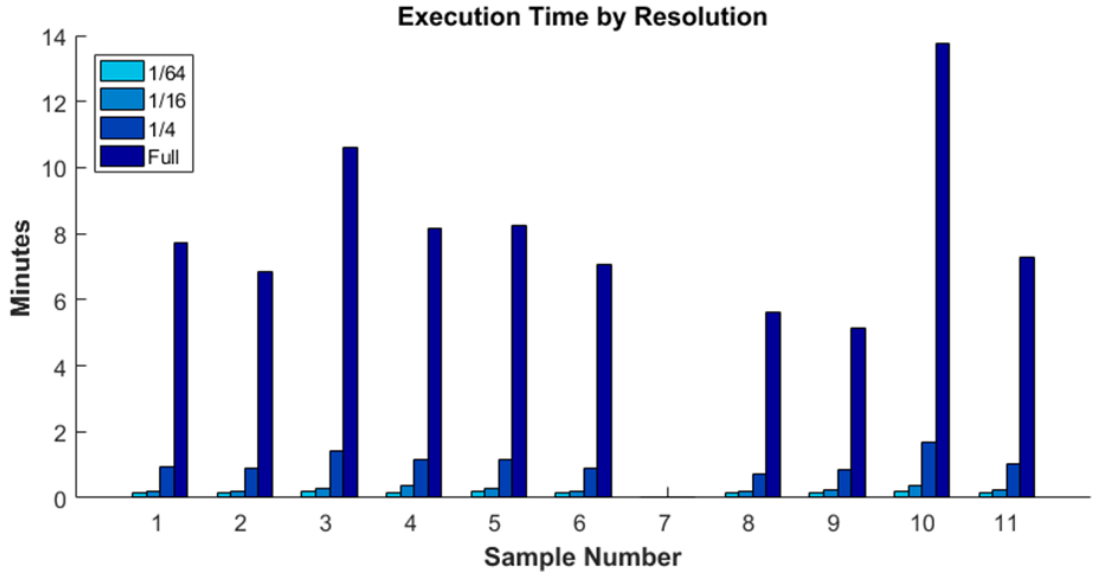

Figure 9. Middle estimate execution time for each sample with increasing resolution. As before, the labels 1/64, 1/16, and 1/4 represent the scaled reduction in pixels along both dimensions.

3.2 Comparison with Aperio ImageScope

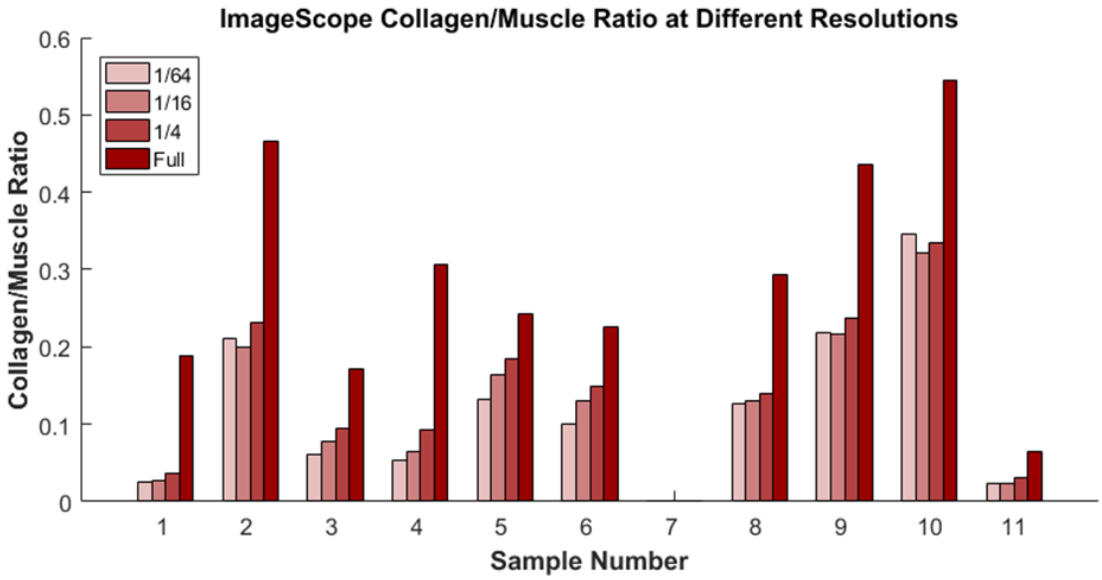

Figure 10. Collagen to muscle ratio for each sample with increasing resolution.

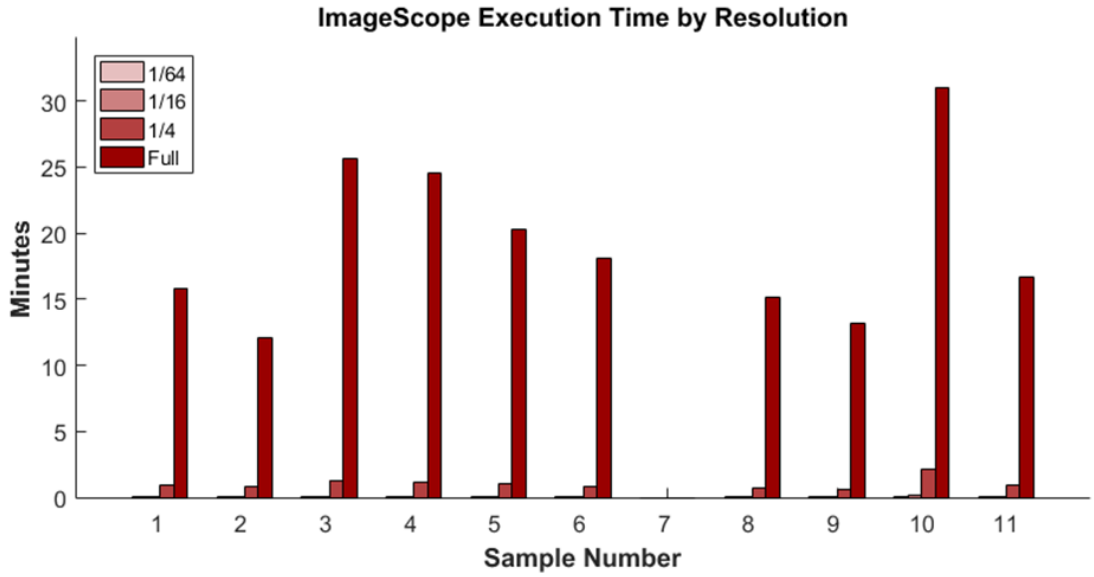

Figure 11. Middle estimate execution time for each sample with increasing resolution.

The results of the custom algorithm were compared against the “Positive Pixel Count” algorithm provided in the repurposed immunohistochemistry software, Aperio ImageScope version 12.1.0.5029 by Leica Biosystems, used in pathological studies. The thresholds in this software were determined by a licensed pathologist in consultation with ImageScope product support.

Fig. 10 shows the segmentation results for each sample; the ImageScope algorithm does not compute an error estimate. Fig. 11 displays the respective execution times for each sample.

4. DISCUSSION

4.1 Resolution Trends

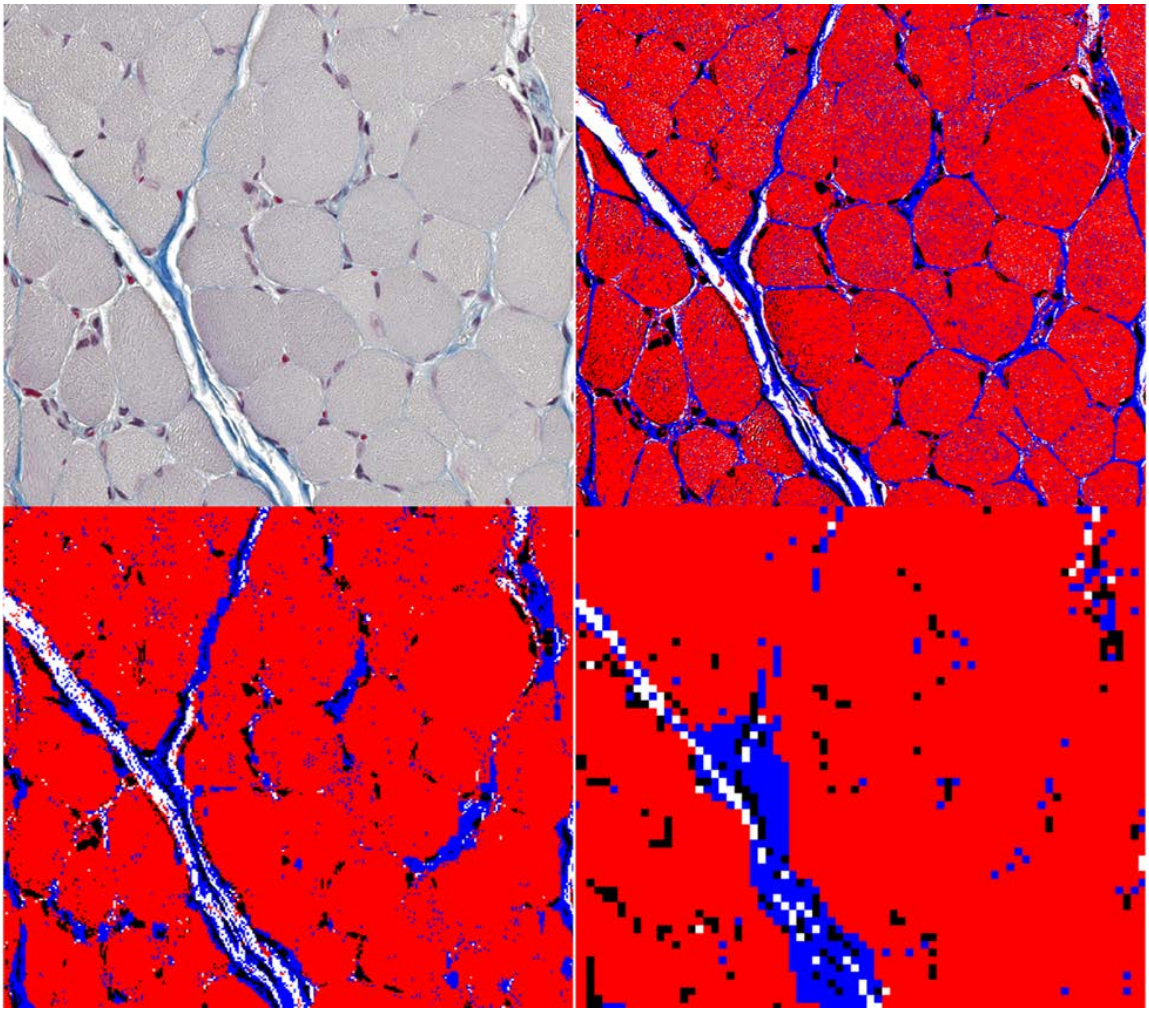

Figure 12. Effects of resolution on segmentation result. Top-Left: selection from sample 4 before segmentation (this sub-image represents about 1/3000th of the total non-background pixels). Top-Right: segmented image at full resolution. Bottom-Left: segmented image at "1/4" resolution. Bottom-Right: segmented image at "1/16" resolution.

The collagen to muscle ratio presented quantitatively in the foregoing section strongly varies according to image resolution. With the custom algorithm presented in this paper, the trend appears approximately positive linear when the resolution increases exponentially by a factor of four. The ImageScope plots show a higher degree of non-linearity.

The explanation for the phenomenon lies in the increasing underestimation of the endomysium at lower resolutions. The narrow collagen borders that form a web-like net between each of the muscle fibers slowly fade away as spatial averaging in the downsampling process effectively filters these fine lines, see Fig. 12. But the increasing visibility of the endomysium at higher zoom levels is not the only effect associated with increased resolution. Fig. 13 illustrates that tissue texture also plays a role at the full, 227nm-per-pixel resolution. What should be classified as muscle fiber is sometimes considered fibrosis during segmentation. This “speckle” pattern overestimation (also visible in the top central region of the images in Fig. 7) is compounded by the misclassification of the degenerating fibers as previously illustrated in Fig. 7. All of these effects—the underestimation of the endomysium and the overestimation of fibrosis associated with the tissue texture and degenerating fibers—were observed in both the custom and “Positive Pixel Count” algorithms.

Not surprisingly, both algorithm execution times increased in an exponential fashion as the number of pixels analyzed increased exponentially.

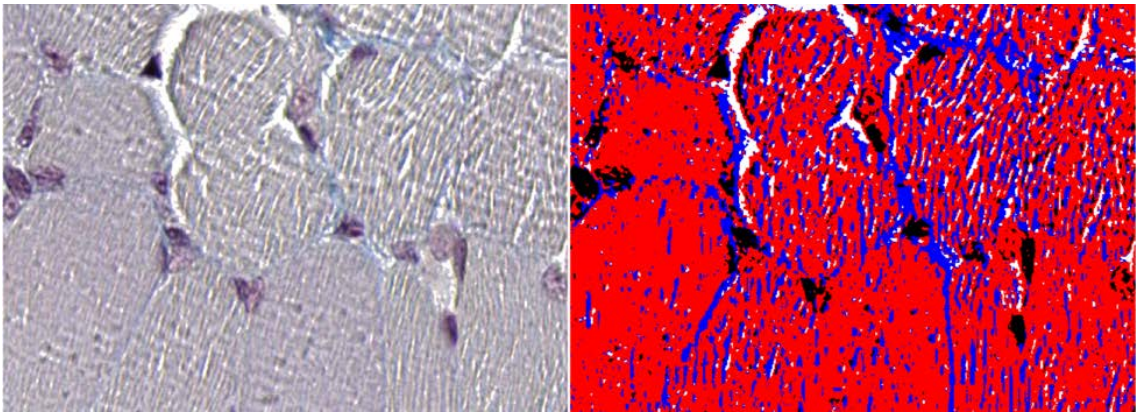

Figure 13. Close-up view of issues that can occur with tissue texture at full resolution. Left: selection from sample 2 before segmentation. Right: segmented image.

4.2 Differences between ImageScope and the Custom Algorithm

The main consistent discrepancy between the ImageScope estimation of tissue categories and the custom algorithm estimate is that the ratio of fibrosis to muscle is significantly higher. While the ImageScope software does not provide an uncertainty metric, it could be said that the threshold errs on the side of fibrosis, showing thicker perimysium estimation between muscle fibers bundles as well as a thicker endomysium between cells, and in general classifying the degenerating fibers as fibrosis. By observation it also has significant overestimation in regards to the issue of tissue texture. By contrast, the custom algorithm aims more to strike a balance between the opposing sources of error as described in the previous section.

In terms of accuracy, the custom algorithm also has the advantage of thresholds adapted to the histogram of the present sample under analysis, whereas the ImageScope threshold is fixed from sample to sample. The latter approach can be problematic when the amount of trichrome stain from sample to sample may have considerable variability.

While care was taken in laboratory procedures to avoid large inconsistencies in staining, inevitably some images and even sub-regions of images simply acquired more stain and appear more blue in general, notwithstanding the tissue composition may be comparable to other samples. The ImageScope segmentations do show what looks like streaks across the images where abnormally high levels of fibrosis are measured that could be an artifact of staining (see Fig. 14), except that the custom algorithm does not show these same streaks. The adaptive histogram-based threshold of the custom algorithm could be one explanation for the difference since the streaks do not occur in all samples in ImageScope, but it may more likely be the method of explicit image partitioning and storage in lossless TIFF format in the custom algorithm that avoids this artifact. How the Positive Pixel Count algorithm processes these immense images is unknown, other than that the directly processed .ndpi file is based on JPEG 2000 compression.

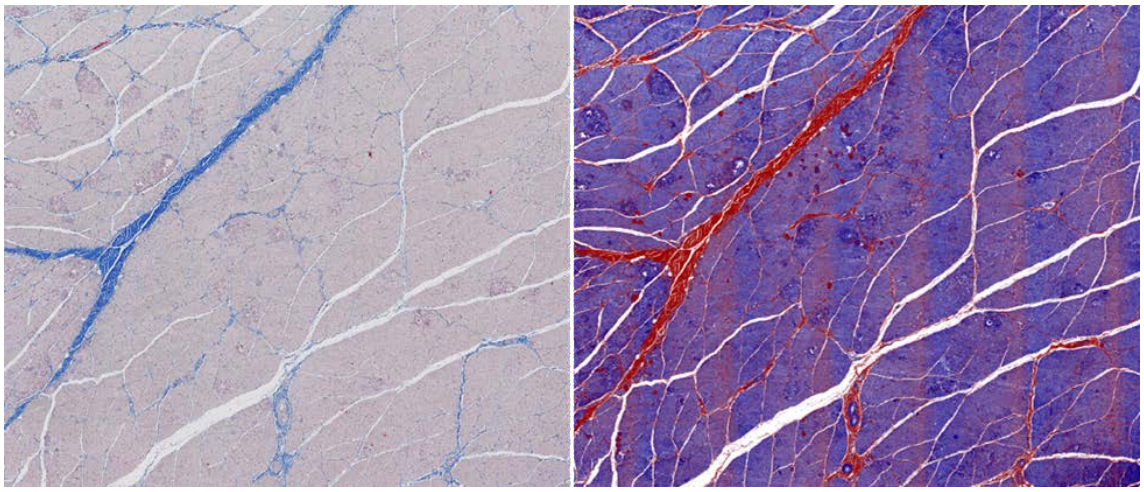

Figure 14. Zoomed-out view of high resolution segmentation results from Aperio ImageScope. Left: image selection from sample 2 before segmentation. Right: vertical red “streaks” stripe the segmented image that do not correspond to actual fibrosis. Note that the ImageScope color-scheme is reverse: blue represents muscle tissue and red fibrosis.

At the lowest 1/64th resolution, ImageScope also had noticeable error in samples 2, 9, and 10 that appeared to be an artifact of poor image downsampling and/or compression. For example, within the unsegmented image in Fig. 15, a thick blue band of fibrosis is visible on the right-hand side. While this infiltration of fibrosis is identified correctly in the segmented image, another obtrusive region of fibrosis is misidentified in the upper central region of the same segmented image. Interestingly enough, these observations of artifact in samples 2, 9, and 10 coincide with aberrations from the steadily downward collagen to muscle ratio trend found in the other samples in Fig. 10.

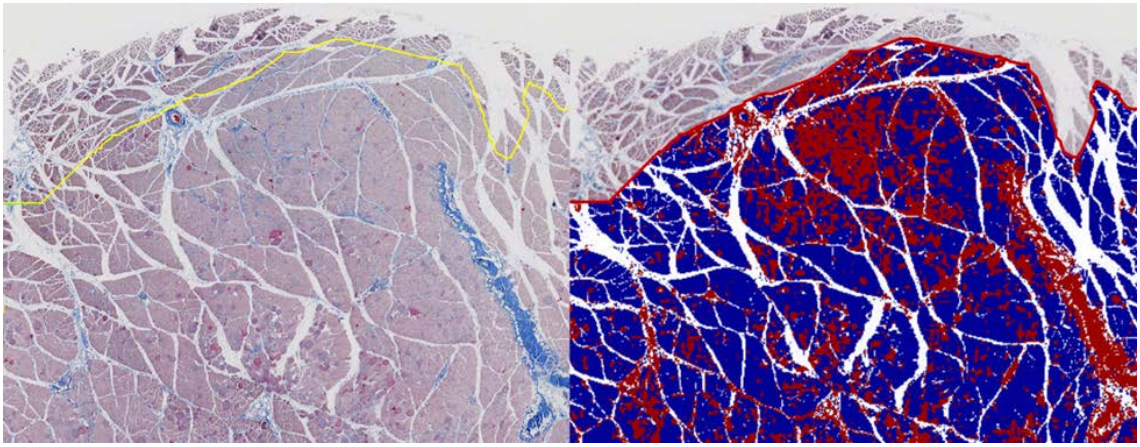

Figure 15. Snapshot from Aperio ImageScope. Left: image selection from sample 10 before segmentation. The yellow line across the top represents the edge of a manually drawn processing region. Right: segmented result at the lowest "1/64th" resolution. Note that the ImageScope color-scheme is reverse: blue represents muscle tissue and red fibrosis.

Another discrepancy between ImageScope and the custom algorithm may be attributed to the custom algorithm's exclusion of the satellite cells which ImageScope generally classified as collagen. While the percentage of tissue that constituted satellite cells was found to be less than 7% in general, and around 3% in the normal dogs, the

tissue in sample 4 was a notable exception. This sample from an affected GRMD animal had a high rate of muscular regeneration and the satellite cells constituted up to 12% of the sample. This created an appreciable discrepancy between the full-resolution results from the custom algorithm versus the segmented ouput of the ImageScope software (compare Fig. 8 and 10).

Is there an optimal or sufficient processing resolution? In this study, qualitative visual inspection of the results showed that issues with image texture and degenerating cells were less pronounced at less than full resolution, presumably because these effects are diminished by spatial averaging associated with downsampling. There is also significant execution time benefits to processing the images even at the next-to-highest resolution studied (908nm per pixel) versus full. Interestingly enough, this particular resolution also showed the highest correlation between the collagen to muscle ratio of the custom algorithm and the ImageScope software with a Pearson's correlation coefficient of 0.9875. The full resolution actually had the lowest correlation coefficient at 0.9336. However, because the endomysium is increasingly underestimated at lower resolutions, for this study the best single estimate for each sample would likely be the high rather than the middle estimate at the 1/4 or 10x resolution.

In terms of robustness, the custom algorithm executes successfully each time and executed in approximately half the time of ImageScope at full resolution for a single estimate—considering the case when, for example, only the middle estimate is desired and error estimates are not needed. Such is the case when the segmented image itself is the desired output, rather than the statistical estimates, as in the application of

registration and comparison with MRI images. When the application is to provide quantitative data for histo-pathological studies, longer computation time can be allocated to obtain the additional high and low error estimates. The total execution time is then approximately 3 times the reported middle estimate time, although no special optimizations were included in the algorithm for this particular case but could be implemented.

The ImageScope software showed slightly faster execution than the custom algorithm at the lower resolutions, however, it crashed repeatedly throughout use by more than one of the authors. A significant disadvantage of the ImageScope software is that it requires manual segmentation of the sample borders, although it does provide a pen tool within the software itself to accomplish this. Manual segmentations in this study took approximately 1-3 minutes per sample, excluding mistakes made during the continuous mouse-button-down dragging of the cursor around the border of the sample (any mistake or premature mouse-button-up required the user to start over). The automated border finding for the custom algorithm took 10-20 seconds depending on the sample image size. More valuable than the time savings seen in this study is that automatic border segmentation allows the creation of a fully automated process for processing potentially hundreds of images in future work.

4.3 Future Work

While effort was made to remove dark artifacts due to excess stain or tissue folding and overlap, further work could be done to identify circulatory or nervous tissue that occasionally presented itself in the sample slides. Fatty deposits also proved difficult

to distinguish from the slide background in these images. This represents a topic of continued research.

Future studies plan to process increasingly more images to include many images per muscle sample. Such studies could enable comparison of segmentation consistency across multiple slides from the same muscle. The novel automatic segmentation algorithm implemented in MATLAB provides scalable functionality and can execute continuously on an arbitrarily large number of samples without human intervention.

5. CONCLUSIONS

The novel algorithm presented in this study provides a robust and effective metric for quantifying otherwise qualitative histopathological image data. Furthermore, it enables histology-based comparisons with images acquired from other modalities such as MRI because its image results are exportable.

The automatic process including automated border finding reduces the time and human effort necessary to produce the quantitative results, even in comparison with industry software.

The adaptive histogram based thresholds help to avoid staining variation from sample to sample. There is also a designed threshold to remove some staining artifacts and the myosatellite cells which create tissue classification ambiguity.

An error estimation technique was also introduced by setting alternative high and low thresholds for over and underestimation values. This allows for better interpretation and utilization of the quantitative data.

The study also shed light on the effect that image processing resolution has on quantitative results. An optimal processing resolution at the 1/4 or 10x resolution was also suggested owing to an increased understanding of the textural and degenerate cell coloration challenges encountered at the full 40x resolution.

Finally, the algorithm implementation in MATLAB provides a readily adaptable development platform that can execute continuously and without human intervention on large sample sizes for future, more extensive studies.

REFERENCES

[1] J. Wang, Z. Fan, K. Vandenborne, G. Walter, Y. Shiloh-Malawsky, *et al.*, "A computerized MRI biomarker quantification scheme for a canine model of Duchenne muscular dystrophy," *International Journal of Computer Assisted Radiology and Surgery*, vol. 8, no. 5, Jan. 2013.

[2] M. Koenig, E. P. Hoffman, C. J. Bertelson, A. P. Monaco, C. Feener, *et al.*, "Complete cloning of the duchenne muscular dystrophy (DMD) cDNA and preliminary genomic organization of the DMD gene in normal and affected individuals," *Cell*, vol. 50, no. 3, pp. 509–517, Jul. 1987.

[3] J. W. McGreevy, C. H. Hakim, M. A. McIntosh, and D. Duan, "Animal models of Duchenne muscular dystrophy: from basic mechanisms to gene therapy," *Disease Models & Mechanisms*, no. 8, pp. 195–213, 2015.

[4] E. P. Hoffman, R. H. Brown, and L. M. Kunkel, "Dystrophin: The protein product of the duchenne muscular dystrophy locus," *Cell*, vol. 51, no. 6, pp. 919–928, Dec. 1987.

[5] Y. Kharraz, J. Guerra, P. Pessina, A. L. Serrano, and P. Muñoz-Cánoves, "Understanding the process of fibrosis in Duchenne muscular dystrophy," *BioMed Research International*, vol. 2014, May 2014.

[6] A. M. Lavorato-Rocha, L. G. Anjos, I. W. Cunha, J. Vassallo, F. A. Soares, *et al.*, "Immunohistochemical assessment of PTEN in vulvar cancer: Best practices for tissue

staining, evaluation, and clinical association," *Methods*, vol. 77–78, pp. 20–24, May 2015.

[7] M. García-Rojo, J. R. Sanches, E. Santa, E. Duran, J. L. Ruiz, *et al.*, "Automated image analysis in the study of lymphocyte subpopulation in eosinophilic oesophagitis," *Diagnostic Pathology*, vol. 9, no. Suppl 1, pp. S7, 2014.

[8] R. Rajandram, N. Y. Yap, J. Pailoor, A. H. Razack, K. L. Ng, *et al.*, "Tumour necrosis factor receptor-associated factor-1 (TRAF-1) expression is increased in renal cell carcinoma patient serum but decreased in cancer tissue compared with normal: Potential biomarker significance," *Pathology*, vol. 46, no. 6, pp. 518–522, Oct. 2014.

[9] C. Marinaccio and D. Ribatti, "A simple method of image analysis to estimate CAM vascularization by APERIO ImageScope software," *The International Journal of Developmental Biology.*, vol. 59, pp. 217–9, Oct. 2015.

[10] L. R. Smith and E. R. Barton, "SMASH – semi-automatic muscle analysis using segmentation of histology: A MATLAB application," *Skeletal Muscle*, vol. 4, no. 1, pp. 21, 2014.

[11] J. Mula, J. D. Lee, F. Liu, L. Yang, and C. A. Peterson, "Automated image analysis of skeletal muscle fiber cross-sectional area," *Innovative Methodology*, vol. 114, no. 1, pp. 148–155, Jan. 2013.

[12] C. Deroulers, D. Ameisen, M. Badoual, C. Gerin, A. Granier, *et al.*, "Analyzing huge pathology images with open source software," *Diagnostic Pathology*, vol. 8, no. 1, pp. 92, 2013.

[13] G. Zack, W. Rogers, and S. Latt, "Automatic measurement of sister chromatid exchange frequency," *The Journal of Histochemistry and Cytochemistry: Official Journal of the Histochemistry Society.*, vol. 25, no. 7, pp. 741–53, Jul. 1977.

[14] S. J. Colley. *Vector Calculus*, 2nd ed. NY: Pearson, 2005, pp. 49.

[15] R. C. Gonzales and R. E. Woods. *Digital Image Processing*, 3rd ed. NJ: Prentice Hall, 2007, pp. 743.

[16] Y. Tanabe, K. Esaki, and T. Nomura, "Skeletal muscle pathology in X chromosome-linked muscular dystrophy (mdx) mouse," *Acta Neuropathologica*, vol. 69, no. 1-2, pp. 91–95, 1986.